Journal of Nuclear Materials 396 (2010) 49–56

Contents lists available at ScienceDirect

Journal of Nuclear Materials

journal homepage: www.elsevier.com/locate/jnucmat

Phase characteristics of a number of U–Pu–Am–Np–Zr metallic alloys for use as fast reactor fuels

Douglas E. Burkes *, J. Rory Kennedy, Thomas Hartmann, Cynthia A. Papesch, Dennis D. Keiser Jr.

Nuclear Fuels and Materials Division, Idaho National Laboratory, P.O. Box 1625, Idaho Falls, ID 83415-6188, USA

ARTICLE INFO

Article history:
Received 12 April 2009
Accepted 20 October 2009

ABSTRACT

Metallic fuel alloys consisting of uranium, plutonium, and zirconium with minor additions of americium and neptunium are under evaluation for potential use to transmute long-lived transuranic actinide isotopes in fast reactors. A series of test designs for the Advanced Fuel Cycle Initiative (AFCI) have been irradiated in the Advanced Test Reactor (ATR), designated as the AFC-1 and AFC-2 designs. Metal fuel compositions in these designs have included varying amounts of U, Pu, Zr, and minor actinides (Am, Np). Investigations into the phase behavior and relationships based on the alloy constituents have been conducted using X-ray diffraction and differential thermal analysis. Results of these investigations, along with proposed relationships between observed behavior and alloy composition, are provided. In general, observed behaviors can be predicted by a ternary U–Pu–Zr phase diagram, with transition temperatures being most dependent on U content. Furthermore, the enthalpy associated with transitions is strongly dependent on the as-cast microstructural characteristics.

1. Introduction

The development of fuel alloys for use in the transmutation of minor actinides (MA), such as americium, neptunium, and curium, is one of the top goals of the Advanced Fuel Cycle Initiative (AFCI) program. Fast reactors are poised to effectively provide long-term management of plutonium and MA, thereby minimizing proliferation risks and waste depository requirements while still generating a respectable amount of heat for energy, hydrogen, or water desalination. Fuels for fast reactors must behave in a benign manner during core transient events, maintain integrity at high burnup, lend themselves to low-loss recycling processes, and be easily fabricated with minimal material loss in a remote handling environment. The application of metal alloy fuels for use in fast reactors for MA transmutation is of particular interest, due to the ease in fabrication, high thermal conductivity, high fissile and fertile density capability, and small Doppler reactivity feedback [1]. Because of this, metal alloy fuels are one of the common fuel types considered for fast reactor recycle. Unfortunately, there is only limited fuel performance data to support the selection of a fuel type for this application.

Thousands of metal fuel pins were fabricated in support of the Experimental Breeder Reactor-II (EBR-II) reactor in Idaho during the 1960s, 70s, and 80s [2]. Several fuel designs (designated as Mark) were explored, including alloys of composition U–5Fs, U–10Zr, and U–Pu–Zr. Only a few irradiation tests were carried out on a U–Pu–Zr fuel alloy that was intended for the conversion of the EBR-II driver core before it was terminally shut down in 1994. Thus, only a limited characterization and performance database is available on these particular alloy systems. These original EBR-II designs have been expanded in the form of Advanced Fuel Cycle (AFC) designs that are based on U–Pu–Zr ternary alloys but contain minor amounts of Am and Cm. To date, a series of compositions has been characterized and irradiated, designated as the AFC-1 and -2 designs.

Beginning-of-life (BOL) phase behavior is an important characteristic to determine and evaluate the performance and behavior of the fuel alloy as a function of irradiation (i.e., operating temperature, fission rate, burnup). It is important to a fuels-development campaign to separate changes that might occur upon irradiation in order to affect fuel fabrication techniques to optimize microstructural characteristics and to relate behavioral differences of well-characterized fuels at BOL and end of life (postirradiation evaluation [PIE]). Furthermore, adequate understanding of phase behavior can be a powerful tool in the development and verification of predictive modeling tools, both in terms of fabrication processes and irradiation performance. Thus, an adequate understanding of how constituents affect the thermal and phase behaviors of metallic fuel alloys is important for continued development of fast reactor concepts.

2. Experimental materials and methods

Six metal alloys were investigated based on compositions used in the AFC-1 and AFC-2 irradiation test designs. Although not

* Corresponding author. Tel.: +1 208 533 7984; fax: +1 208 533 7863.
E-mail address: Douglas.Burkes@inl.gov (D.E. Burkes).

0022-3115/$ - see front matter © 2009 Elsevier B.V. All rights reserved.
doi:10.1016/j.jnucmat.2009.10.053

Table 1
Percentage of alloying metals that comprise the experimental fuels for this study (nominal weight percentages) used in the AFC-1 and AFC-2 irradiation test designs.

Alloy	U_{tot}[a]	Pu_{tot}[b]	Am	Np	Zr	AFCI ID
A	60	20	3	2	15	AFC-2-A1
B	43	30	5	2	20	AFC-2-A6
C	40	34	4	2	20	AFC-1-MG
D	35	29	4	2	30	AFC-1-MI
E	35	28	7	-	30	AFC-1-MF
F	30	25	3	2	40	AFC-1-MH

[a] U_{tot} is composed of ^{235}U and ^{238}U, with minor amounts of the isotopes ^{234}U and ^{236}U.
[b] Pu_{tot} is composed of ^{239}Pu and ^{240}Pu, with minor amounts of the isotopes ^{238}Pu, ^{241}Pu, and ^{242}Pu.

anticipated to affect the properties measured herein, the U used in these alloys had varying enrichment and contained minor amounts of isotopes (^{234}U and ^{236}U) other than the target isotopes (^{235}U and ^{238}U). The alloys are defined in Table 1 along with the alloy letter that will be used to define the composition throughout the paper. Composition and preparation of the alloys in this study are the same as those employed to fabricate fuel slugs for the AFC-1 and AFC-2 irradiation test designs, i.e., the phase characteristics of these alloys are representative of the slugs subjected to irradiation.

2.1. Alloy and sample preparation

An arc-melting process was used to melt and cast the metallic fuel alloys as defined in Table 1 [3]. Right cylindrical fuel slugs approximately 5 mm in diameter and approximately 20 mm in length were cast from the homogenized melt using quartz molds. The casting was removed by breaking the quartz mold, followed by sectioning the slug into multiple samples, each approximately 1 mm thick, employing a low-speed, diamond-blade saw. The resultant samples were used for thermal and phase characterization. Further sample preparation ensured a flat surface for maximum contact (differential scanning calorimeter [DSC]) and X-ray diffraction (XRD). A sample from one slug casting was used for thermal analysis, while three samples from three separate slug castings were used for phase determination. An example microstructure for each alloy is provided in Fig. 1 [4,5]. The photomicrograph reveals the presence of a mixture of light and dark grey phases along with black, globular inclusions distributed randomly throughout the multi-phase mixture. The presence of a multi-phase mixture is consistent with previous studies on U–Pu–Am–Np–Zr alloys, while the black, globular inclusions are consistent with oxygen-stabilized α-Zr inclusions commonly observed for U–Pu–Zr ternaries [4]. The volume fraction of the inclusions varies directly with oxygen concentration, dissolving up to 4 wt.% uranium and 2.5 wt.% plutonium [6].

2.2. X-ray diffraction and phase identification

A minimum of two samples for phase determination was placed into a machined groove in a polycarbonate sample holder that measured 20 mm long by 5 mm wide by 5 mm deep. The samples were placed side by side in a layer of vacuum grease that filled the machined groove. The samples were pressed into the vacuum grease using a flat surface to ensure uniform sample exposure to the X-ray beam. AFC-1 alloys were measured with an industrial Al internal standard, while AFC-2 alloys were measured with a LaB_6 (SRM 660a) internal standard. The sample holder was placed in a containment chamber with a 180° beryllium window allowing for analysis of radioactive materials. X-ray diffraction patterns were obtained on the samples simultaneously employing a Scintag X1 powder diffractometer with a theta–theta goniometer configuration using copper $K\alpha_{1,2}$ radiation at room temperature. The scan was conducted in a continuous scanning mode at 0.5° min^{-1} from 20 to 120° 2θ. The XRD data were evaluated using Rietveld analysis (Bruker AXS Topas3). X-ray diffraction profiles of measured diffracted intensities were fitted using symmetrical Pseudo-Voigt (Pearson VII) profile functions.

2.3. Thermal analysis

Transition temperatures and enthalpies of transition were determined employing a NETZSCH differential scanning calorimeter/thermogravimetric analyzer (DSC/TGA) model STA 409 PC. Pt–Rh crucibles coated with yttria were used to hold the alloy sample. Ultra-high purity argon cover gas passed through an oxygen gettering furnace (OxyGon Industries Inc., Model OG-120M) was used to conduct the experiments. Oxygen impurity levels were in the sub ppb range based on the measurability of the furnace. Flow rates of 50 mL min^{-1} and 20 mL min^{-1} were established for the instrument balance and sample furnace. Three consecutive DSC runs were conducted from ambient temperature to approximately 800 °C, each followed by controlled cooling to ambient temperature at a rate of 10° min^{-1}. Data was collected during both heating and cooling. Transition onset and finish temperatures were determined using NETZSCH peak deconvolution software. Enthalpies of transition were determined by integrating the full area under each transition as determined by the peak deconvolution software from transition start to transition finish.

3. Results

3.1. Phase diagram development

A phase diagram that represents the five components of the alloys investigated here is not available, nor is it straightforward enough to represent these components in only two or even three dimensions. However, the five components can be reduced to a three component system consisting of U–Pu–Zr so that phase relationships can be extrapolated. Theoretically, minimal solubility exists between U and Am, especially at low temperatures [7], while broad mutual solubility exists between Pu and Am [8]. For this reason, the Am content of the metal alloys can be summed with the Pu content. Likewise, Np has been observed to have mutual solubility in both U and Pu [8], so that the Np content of the metal alloys can be evenly divided between the U and Pu contents. Therefore, the Alloy-A (U–20Pu–3Am–2Np–15Zr) reduces to U–24Pu–15Zr; Alloy-B (U–30Pu–5Am–2Np–20Zr) reduces to U–36Pu–20Zr; Alloy-C (U–34Pu–4Am–2Np–20Zr) reduces to U–39Pu–20Zr; Alloy-D (U–29Pu–4Am–2Np–30Zr) reduces to U–34Pu–30Zr; Alloy-E (U–28Pu–7Am–30Zr) reduces to U–35Pu–30Zr; and Alloy-F (U–25Pu–3Am–2Np–40Zr) reduces to U–29Pu–40Zr.

Isothermal sections of the U–Pu–Zr system are available from published literature at 773 K, 823 K, 853 K, 868 K, and 913 K [6]. These diagrams will be the cornerstone for the analysis of the thermal and XRD observations and have been reproduced in Fig. 2 indicating the position of the reduced composition for each alloy. Furthermore, a room temperature ternary phase diagram can be constructed by extrapolation from the isothermal section at 773 K and the three binary diagrams available (U–Pu, Pu–Zr, and U–Zr) [8]. The extrapolated room temperature ternary phase diagram is provided in Fig. 3 with the reduced composition position marked for each alloy. This diagram must only be considered as an approximation owing to the lower temperatures resulting from the extrapolated behavior, so that many of the phase boundaries may not represent true behavior.

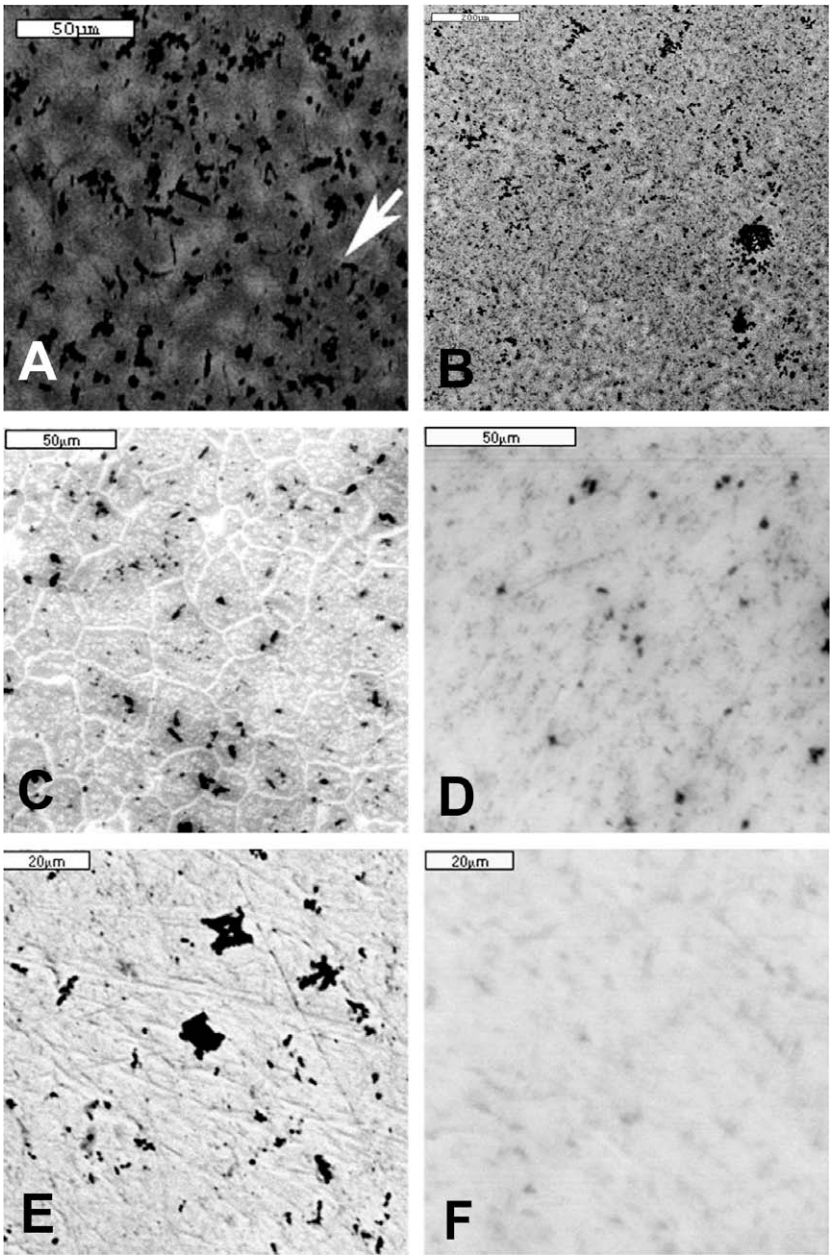

Fig. 1. Sample microstructures of the AFC-1 and AFC-2 alloys. The letter in each photomicrograph corresponds to the alloy composition listed in Table 1. All images were taken in backscattered electron mode in a scanning electron microscope. The black, globular inclusions in each photomicrograph are the oxygen-stabilized α-Zr phase.

Based on observation of the extrapolated room temperature phase diagram, each alloy consists of mainly two phases: δ-(U,Pu)Zr_2 and ζ-(U,Pu). In the case of Alloy-A, it is possible that minor amounts of α-U could be present. Approximated tie lines were placed through each composition from the Zr corner of the diagram to the U/Pu side of the diagram, thus creating a binary slice. The tie lines were used to approximate the amount of δ-(U,Pu)Zr_2 and ζ-(U,Pu) phases present in each alloy. A summary of the predicted phase amounts is provided in Table 2.

Obviously, as the amount of Zr increased for each alloy, the amount of δ-(U,Pu)Zr_2 phase correspondingly increased, while the amount of ζ-(U,Pu) decreased, relatively independent of the Pu concentration. Observation of the reduced alloy compositions for Alloys-A, -B, and -C in Fig. 2 shows that these alloys are expected to undergo three-phase transitions: (i) $\zeta + \delta \rightarrow \delta + \zeta + \gamma$; (ii) $\delta + \zeta + \gamma \rightarrow \zeta + \gamma$; and (iii) $\zeta + \gamma \rightarrow \gamma$. Observation of the reduced alloy compositions for Alloys-D and -E in Fig. 2 shows that these alloys are expected to undergo three different phase transitions: (i) $\delta + \zeta \rightarrow \delta + \zeta + \eta$; (ii) $\delta + \zeta + \eta \rightarrow \delta + \eta + \gamma$; and (iii) $\delta + \eta + \gamma \rightarrow \gamma$. Finally, observation of the reduced alloy composition for Alloy-F in Fig. 2 shows that the alloy is expected to undergo yet again three different phase transitions: (i) $\delta + \zeta \rightarrow \delta + \eta + \gamma$; (ii) $\delta + \eta + \gamma \rightarrow \delta + \gamma$; and (iii) $\delta + \gamma \rightarrow \gamma$, with the reduced alloy composition falling very close to the $\delta + \zeta/\delta + \zeta + \eta$-phase boundary at 773 K.

3.2. X-ray diffraction and phase identification

X-ray diffraction patterns for each of the metallic alloys investigated are provided in Fig. 4. The samples of the alloys show some surface texture generated from the sample preparation methods, i.e., low-speed sectioning of thin slices from cast fuel slugs. In addi-

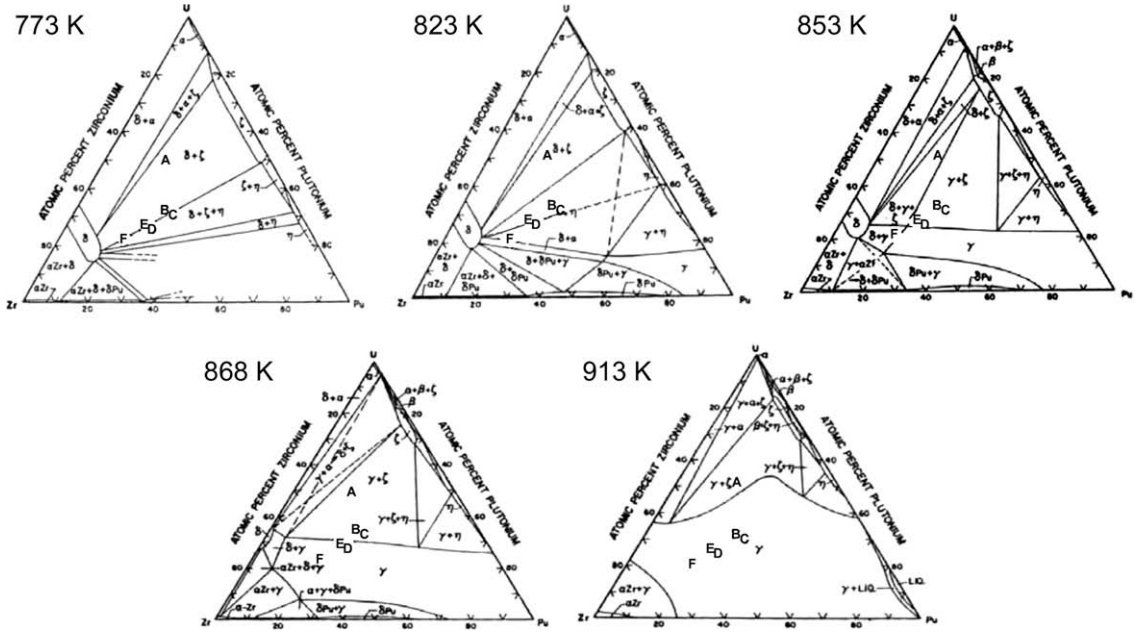

Fig. 2. Ternary U–Pu–Zr phase diagrams taken at isothermal sections of 773 K, 823 K, 853 K, 868 K, and 913 K, after Ref. [6]. The reduced composition (in terms of U–Pu–Zr) for each alloy is marked in each diagram.

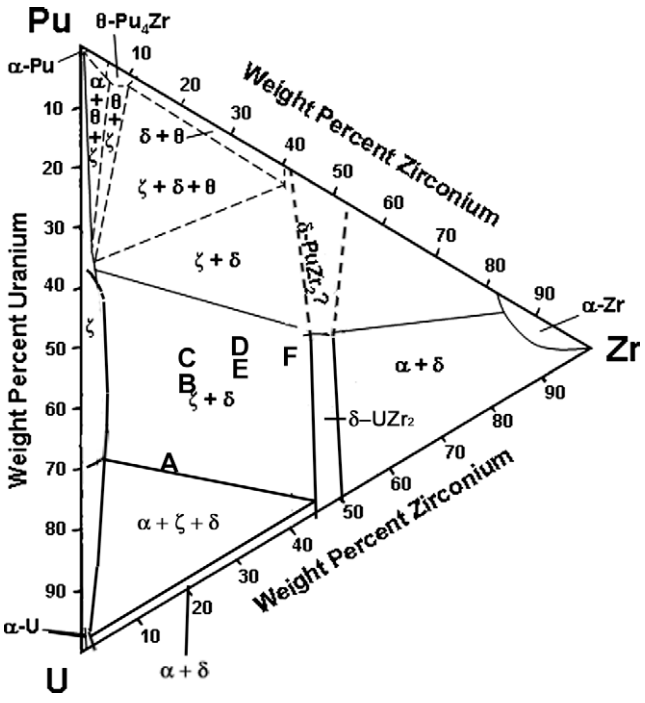

Fig. 3. A room temperature U–Pu–Zr ternary phase diagram estimated from the five isothermal sections from Ref. [6] and the three binary phase diagrams of the elements involved. The reduced composition of each alloy is marked on the diagram.

Table 2
Approximate phase contents for each alloy as determined from a binary slice established at the Zr corner of the ternary phase diagram in Fig. 3.

Alloy	Binary slice	δ-(U,Pu)Zr_2 (wt.%)	ζ-(U,Pu) (wt.%)
A	$Zr–U_{0.73}Pu_{0.27}$	13	87
B	$Zr–U_{0.57}Pu_{0.43}$	38	62
C	$Zr–U_{0.53}Pu_{0.47}$	40	60
D	$Zr–U_{0.50}Pu_{0.50}$	65	35
E	$Zr–U_{0.50}Pu_{0.50}$	70	30
F	$Zr–U_{0.53}Pu_{0.47}$	90	10

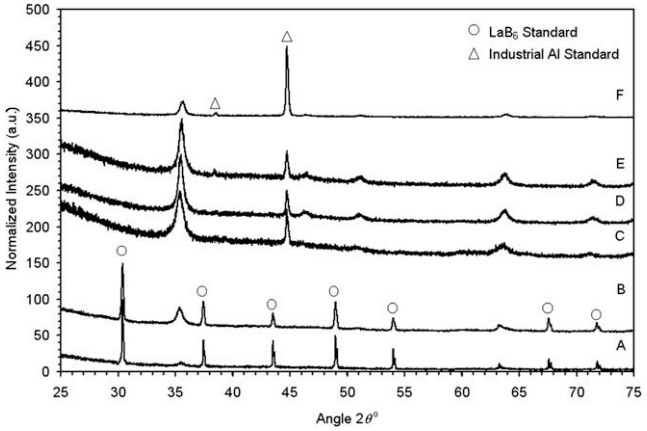

Fig. 4. X-ray diffraction patterns for the AFC-1 and AFC-2 metallic fuel alloys measured with either LaB_6 (SRM 660a) or industrial Al internal standard. Alloy-A is at the bottom, and alloys progress accordingly to F at the top.

tion, significant peak broadening is observed due to the nature of the samples, i.e., monolithic samples and not powder, due to the relatively small sample size of randomly oriented crystallites in a monolith. The Rietveld analysis accounted for these effects in both the standard and as-measured phases if needed, although any significant texture effects will produce large standard derivations in the quantitative phase analysis.

In order to effectively analyze the diffraction patterns with Rietveld, a sufficient knowledge of what phases are expected is necessary. Previous literature on similar U–Pu–Zr systems has suggested the presence of not only the δ-(U,Pu)Zr_2 and ζ-(U,Pu) phases, but also a non-equilibrium γ-U phase. Depending on the particular alloy, some minor amounts of α-U also might be present. The Rietveld analysis was conducted assuming that rapid quenching of

the as-cast alloy results in a non-equilibrium microstructure, consisting of the δ-phase, ζ-phase, α-phase, and γ-phase. In addition, the atomic structures of the δ-(U,Pu)Zr_2 and ζ-(U,Pu) phases were estimated from values available in published literature on the binary systems [9,10]. The presence of oxygen-stabilized α-Zr was not accounted in the Rietveld analysis. Theoretical calculations based on the amount of major phases present suggests that α-Zr in only one of the alloys (Alloy-A) would have been sufficiently high enough to have been detected by XRD (5 vol.% in the sample) within a reasonable degree of certainty. Furthermore, the amount of α-Zr present in the alloy system is dependent upon the casting conditions, unlike the presence of major phases dependent upon alloy composition. These conditions are relatively variable in nature given the method, arc-melting and casting, employed to fabricate the samples. Relatively low refinement residuals, ranging from 6.3 to 14.1%, were obtained from the Rietveld analysis. An example of a refined Rietveld diffraction pattern for Alloy-A is provided in Fig. 5.

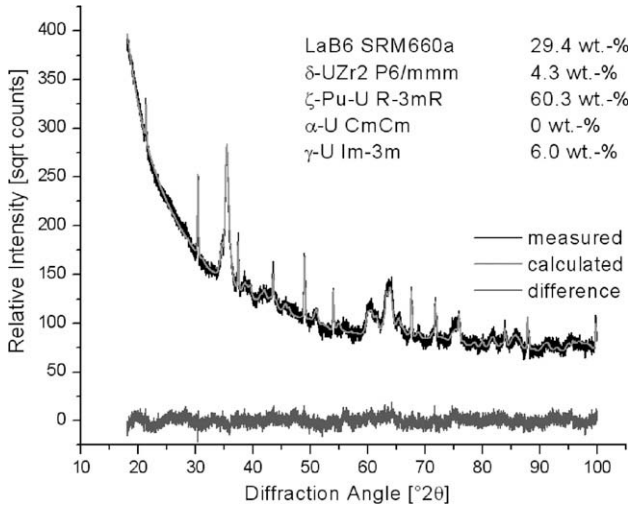

Fig. 5. Example of a refined Rietveld diffraction pattern for Alloy-A. Note the peaks from 60–66° 2θ that are characteristic of the ζ-phase.

Impurities, such as oxygen and nitrogen, can have a significant impact on the limits of the δ-phase and have been offered as the explanation in the phase boundary discrepancies. The structure of the δ-phase can be challenging to confirm because of prospective texture, fairly broad profile functions, and the relatively small quantity of the phase in the alloys. A summary of the quantified phase amounts is provided in Table 3, followed by the refined lattice parameter calculations for each phase and alloy in Table 4.

In general, the phase contents determined from the Rietveld refinement are in relatively good agreement with those values predicted from the constructed room temperature ternary phase diagram in Fig. 3. In some cases, a decrease in the presence of non-equilibrium γ-U phase (e.g., through post-cast anneal treatment), such as that for Alloys-A and -B, would most likely increase the relative amounts of equilibrium ζ-(U,Pu) and δ-(U,Pu)Zr_2. The presence of the high-temperature γ-phase results from a non-equilibrium phase assemblage upon relatively rapid quenching of the alloys. Furthermore, distribution of the elements in the phases is not uniform and will ultimately result in the varying amount of phases, e.g., Zr-rich δ-(U,Pu)Zr_2, Pu-rich ζ-(U,Pu). The δ-(U,Pu)Zr_2 phase has extensive solubility for Pu, the ζ-(U,Pu) phase is capable of dissolving up to 5 at.% Zr, and the *bcc* γ-U phase has a complete solid solubility for both *bcc* ε-Pu and *bcc* β-Zr [6].

3.3. Thermal properties

Sample heating and cooling curves obtained from the differential thermal analysis (DTA) measurement for Alloy-A are provided in Fig. 6. Observation of the figure reveals repeatable and reproducible traces for the alloy. The first DTA run is slightly different than the subsequent two runs, apparently resulting from an annealing effect because these alloys were not heat treated prior to measure-

Table 3
Approximate phase contents for the AFC-1 and AFC-2 metal alloys obtained from Rietveld refinement. Contents were calculated excluding the quantitative amount internal standard.

Alloy	ζ-(U,Pu) (%)	δ-(U,Pu)Zr_2 (%)	α-U (%)	γ-U (%)	Refinement residual R_{wp} (%)
A	85.5	6.1	–	8.4	6.47
B	56.8	28.0	2.2	13.1	6.29
C	50.0	49.9	0.1	–	9.34
D	11.4	88.5	0.1	–	11.09
E	27.2	69.5	2.1	1.2	9.87
F	16.4	82.0	1.6	–	14.06

Table 4
Refined lattice parameters of the AFC-1 and AFC-2 metal alloys for the phases presented in Table 3.

Alloy	ζ-(U,Pu) (Å)	δ-(U,Pu)Zr_2 (Å)	α-U (Å)	γ-U (Å)
A	a = 10.718 ± 0.001 α = 89.42 ± 0.01	a = 5.057 ± 0.005 c = 3.102 ± 0.004	n/a	a = 3.592 ± 0.002
B	a = 10.744 ± 0.003 α = 89.35 ± 0.04	a = 5.057 ± 0.003 c = 3.113 ± 0.002	a = 2.844 ± 0.003 b = 5.861 ± 0.006 c = 5.136 ± 0.005	a = 3.596 ± 0.001
C	a = 10.723 ± 0.004 α = 90.28 ± 0.07	a = 5.085 ± 0.002 c = 3.110 ± 0.002	n/a	n/a
D	a = 10.686 ± 0.008 α = 89.36 ± 0.08	a = 5.059 ± 0.001 c = 3.099 ± 0.001	n/a	n/a
E	a = 10.692 ± 0.006 α = 90.52 ± 0.08	a = 5.062 ± 0.001 c = 3.092 ± 0.001	a = 2.765 ± 0.004 b = 5.654 ± 0.016 c = 4.885 ± 0.002	a = 3.990 ± 0.008
F	a = 10.685 ± 0.003 α = 89.69 ± 0.03	a = 5.048 ± 0.001 c = 3.105 ± 0.001	a = 2.763 ± 0.002 b = 5.597 ± 0.008 c = 5.024 ± 0.007	n/a

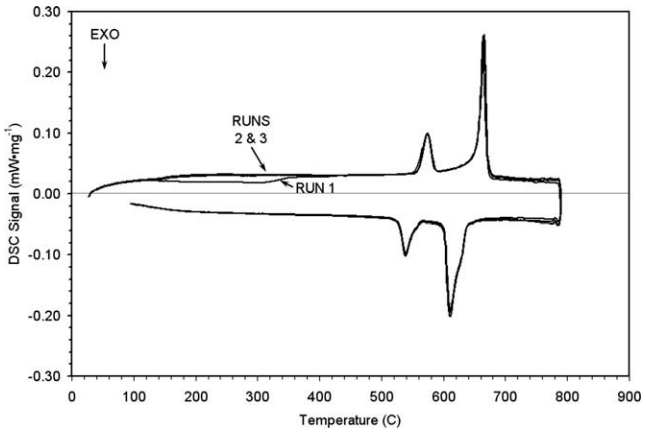

Fig. 6. Sample heating and cooling traces obtained from the DTA measurement on the as-cast Alloy-A.

ment. This is supported by the observation that the same discrepancy between the three runs does not appear upon cooling. Each alloy measured displayed very similar characteristics. During the runs for each alloy, there were very obvious, distinct transitions that were reversible upon cooling. The alloys all show similar features; however, the sharpness, strength, and number of phase transition peaks varied slightly depending on the alloy composition. Typically, a very strong or sharp peak would suggest either a single phase transition or a transition through a very narrow phase field. A broad or weak peak would suggest a transition through a wide phase field, or overlap of two close, consecutive phase transitions. In all cases, the cooling curves appear to resolve the more complex phase behavior than that observed upon heating.

In each case, the DTA traces did not reveal the expected, individual phase transitions predicted by the ternary phase diagrams of Fig. 2. Rather, one or two convoluted transitions, depending on the alloy composition, were observed upon both heating and cooling. Based on the phase transitions predicted by the ternary phase diagram development and analysis, initial guesses for onset of phase transitions were selected based on the transition temperature ranges. The DTA peaks were fit to a Fraser-Suzuki profile that allowed a variable amount of asymmetry in the curve [11]. An example of a deconvoluted DTA trace for Alloy-A upon heating and cooling is provided in Fig. 7. Deconvolution of the DTA traces produced relatively high correlation coefficients of 0.9964 or better. From the deconvoluted peaks, values for the onset and end-

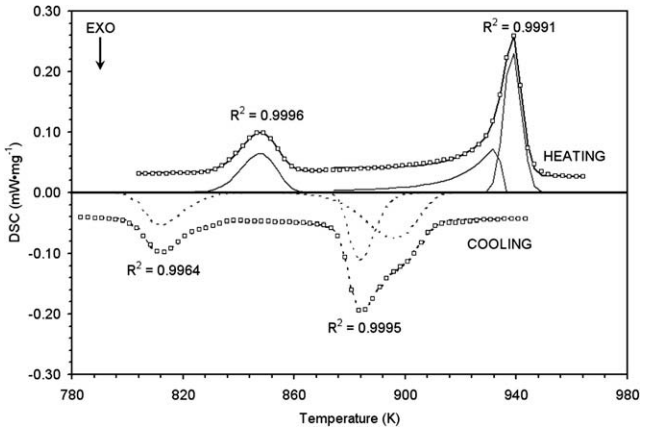

Fig. 7. Deconvoluted differential scanning calorimetry trace for Alloy-A. The anticipated transitions (3) could be reasonably separated from the experimental data with correlation coefficients listed on the figure.

of-phase transitions, along with the enthalpy associated with the transition, can be determined. Deconvolution was performed on each alloy, except Alloy-E, for both heating and cooling with results presented in Tables 5–9. Deconvolution on Alloy-E was not performed because the alloy is very similar to that of Alloy-D, with the exception that Alloy-E contains more Am and no Np compared to Alloy-D, because analysis is based on reduction to three components, rather than four or five. Included on each table are the predicted phase transition temperature ranges obtained from the U–Pu–Zr ternary diagrams.

All transition temperatures obtained from deconvolution of the DTA peaks fall within the predicted transition temperature ranges based on the information presented in Tables 5–9. With the exception of Alloy-C, the transition temperatures might fall slightly outside the predicted temperature range because of super-heating/-cooling effects. These could be effectively dealt with by slowing the heating rate of the sample, which also would help resolve

Table 5
Transition temperatures (T_{tr}) and enthalpies of transition (ΔH_{tr}) determined from differential scanning calorimetry upon heating and cooling of Alloy-A (U–20Pu–3Am–2Np–15Zr).

Predicted			
Transition	$\delta+\zeta \rightarrow \delta+\zeta+\gamma$	$\delta+\zeta+\gamma \rightarrow \zeta+\gamma$	$\zeta+\gamma \rightarrow \gamma$
T_{tr} (K)	823–853	853–868	>913
Heating			
Transition	$\delta+\zeta \rightarrow \delta+\zeta+\gamma$	$\delta+\zeta+\gamma \rightarrow \zeta+\gamma$	$\zeta+\gamma \rightarrow \gamma$
T_{tr} (K)	833 ± 1.4	920 ± 4.0	933 ± 1.1
ΔH_{tr} (J g^{-1})	6.0 ± 0.31	8.6 ± 0.55	10.1 ± 0.50
Cooling			
Transition	$\delta+\zeta+\gamma \rightarrow \delta+\zeta$	$\zeta+\gamma \rightarrow \delta+\zeta+\gamma$	$\gamma \rightarrow \zeta+\gamma$
T_{tr} (K)	829 ± 0.0	894 ± 0.5	912 ± 0.6
ΔH_{tr} (J g^{-1})	−5.9 ± 0.24	−7.9 ± 0.35	−10.9 ± 0.24

Table 6
Transition temperatures (T_{tr}) and enthalpies of transition (ΔH_{tr}) determined from differential scanning calorimetry upon heating and cooling of Alloy-B (U–30Pu–5Am–2Np–20Zr).

Predicted			
Transition	$\delta+\zeta \rightarrow \delta+\zeta+\gamma$	$\delta+\zeta+\gamma \rightarrow \zeta+\gamma$	$\zeta+\gamma \rightarrow \gamma$
T_{tr} (K)	773–823	823–853	868–913
Heating			
Transition	$\delta+\zeta \rightarrow \delta+\zeta+\gamma$	$\delta+\zeta+\gamma \rightarrow \zeta+\gamma$	$\zeta+\gamma \rightarrow \gamma$
T_{tr} (K)	826 ± 2.6	879 ± 7.2	912 ± 12.5
ΔH_{tr} (J g^{-1})	15.3 ± 1.08	7.5 ± 1.98	4.2 ± 1.67
Cooling			
Transition	$\delta+\zeta+\gamma \rightarrow \delta+\zeta$	$\zeta+\gamma \rightarrow \delta+\zeta+\gamma$	$\gamma \rightarrow \zeta+\gamma$
T_{tr} (K)	819 ± 0.6	877 ± 1.2	896 ± 0.2
ΔH_{tr} (J g^{-1})	−16.0 ± 0.14	−8.9 ± 0.34	−5.9 ± 0.29

Table 7
Transition temperatures (T_{tr}) and enthalpies of transition (ΔH_{tr}) determined from differential scanning calorimetry upon heating and cooling of Alloy-C (U–34Pu–4Am–2Np–20Zr).

Predicted			
Transition	$\delta+\zeta \rightarrow \delta+\zeta+\gamma$	$\delta+\zeta+\gamma \rightarrow \zeta+\gamma$	$\zeta+\gamma \rightarrow \gamma$
T_{tr} (K)	773–823	823–853	868–913
Heating			
Transition	$\delta+\zeta \rightarrow \delta+\zeta+\gamma$	$\delta+\zeta+\gamma \rightarrow \zeta+\gamma$	$\zeta+\gamma \rightarrow \gamma$
T_{tr} (K)	815 ± 2.2	837 ± 10.9	889 ± 3.6
ΔH_{tr} (J g^{-1})	7.2 ± 1.70	2.4 ± 1.56	3.6 ± 0.41
Cooling			
Transition	$\delta+\zeta+\gamma \rightarrow \delta+\zeta$	$\zeta+\gamma \rightarrow \delta+\zeta+\gamma$	$\gamma \rightarrow \zeta+\gamma$
T_{tr} (K)	804 ± 1.2	866 ± 10.3	883 ± 0.5
ΔH_{tr} (J g^{-1})	−9.2 ± 0.19	−4.0 ± 1.57	−2.9 ± 1.60

Table 8
Transition temperatures (T_{tr}) and enthalpies of transition (ΔH_{tr}) determined from differential scanning calorimetry upon heating and cooling of Alloy-D (U–29Pu–4Am–2Np–30Zr).

Predicted			
Transition	$\delta+\zeta\rightarrow\delta+\zeta+\gamma$	$\delta+\zeta+\gamma\rightarrow\zeta+\gamma$	$\zeta+\gamma\rightarrow\gamma$
T_{tr} (K)	773–823	823–853	853–868
Heating			
Transition	$\delta+\zeta\rightarrow\delta+\zeta+\gamma$	$\delta+\zeta+\gamma\rightarrow\zeta+\gamma$	$\zeta+\gamma\rightarrow\gamma$
T_{tr} (K)	820 ± 1.4	832 ± 3.4	855 ± 0.5
ΔH_{tr} (J g^{-1})	5.8 ± 2.27	13.7 ± 2.13	3.8 ± 1.23
Cooling			
Transition	$\delta+\zeta\rightarrow\delta+\zeta+\gamma$	$\delta+\zeta+\gamma\rightarrow\zeta+\gamma$	$\zeta+\gamma\rightarrow\gamma$
T_{tr} (K)	796 ± 0.6	835 ± 14.5	836 ± 0.3
ΔH_{tr} (J g^{-1})	−2.0 ± 0.86	−8.0 ± 3.02	−13.5 ± 2.17

Table 9
Transition temperatures (T_{tr}) and enthalpies of transition (ΔH_{tr}) determined from differential scanning calorimetry upon heating and cooling of Alloy-F (U–25Pu–3Am–2Np–40Zr).

Predicted			
Transition	$\delta+\zeta\rightarrow\delta+\eta+\gamma$	$\delta+\eta+\gamma\rightarrow\delta+\gamma$	$\delta+\gamma\rightarrow\gamma$
T_{tr} (K)	773–823	823–853	853–868
Heating			
Transition	$\delta+\zeta\rightarrow\delta+\eta+\gamma$	$\delta+\eta+\gamma\rightarrow\delta+\gamma$	$\delta+\gamma\rightarrow\gamma$
T_{tr} (K)	839 ± 1.3	850 ± 3.9	861 ± 3.5
ΔH_{tr} (J g^{-1})	10.1 ± 6.87	11.2 ± 2.53	4.5 ± 0.08
Cooling			
Transition	$\delta+\eta+\gamma\rightarrow\delta+\zeta$	$\delta+\gamma\rightarrow\delta+\eta+\gamma$	$\gamma\rightarrow\delta+\gamma$
T_{tr} (K)	831 ± 0.2	839 ± 0.7	846 ± 0.5
ΔH_{tr} (J g^{-1})	−8.4 ± 1.02	−12.8 ± 0.37	−5.2 ± 4.03

any additional phase relationships not apparent from the current DTA traces. Based on the enthalpies of transition for each alloy, all transitions are reversible, within 1σ. Typically, the total heat exchange is greater during the cooling cycle than on the heating cycle.

4. Discussion

The phase analysis discussion will be broken into two sections, alloys that have less than or equal to 20 wt.% Zr (Alloys-A, -B, and -C), and alloys that have greater than 20 wt.% Zr (Alloys-D, -E, and -F). For the first set (Alloys-A, -B, and -C), the amount of δ-(U,Pu)Zr_2 decreased while the amount of ζ-(U,Pu) increased with increased U contents, and subsequently decreased Pu and Zr contents. Observation of the photomicrographs in Fig. 1 shows that Alloys-A and -B have a significant amount of oxygen-stabilized α-Zr, while Alloy-C has significantly less.

Lawson et al. observed a rhombohedral unit cell with $a_0 = 10.6853$ Å and $\alpha = 89.736°$ for ζ-$Pu_{0.6}U_{0.4}$ [9]. The trend is toward a smaller lattice parameter with increasing U content within the binary U–Pu system [12]. The lattice parameters determined for these alloys are larger than those determined by Lawson et al. [9], suggesting that in each case the alloys are U-lean. Alloy-A and -C have very similar lattice parameters for the ζ-(U,Pu) phase, suggesting that these two are close in composition. Because Alloy-A had more visible oxygen-stabilized α-Zr, it is reasonable that less Zr was available for the δ-(U,Pu)Zr_2 phase compared to that of Alloy-C. Less Zr available for the δ-(U,Pu)Zr_2 phase in Alloy-A is expected to result in less δ-(U,Pu)Zr_2 phase present than predicted and excess U that results in a non-equilibrium γ-U phase. This trend was observed with only 6 wt.% δ-(U,Pu)Zr_2 present, compared to a predicted amount of 13 wt.%, and 8 wt.% γ-U.

In addition, because of the similarities between Alloy-A and -C for the ζ-(U,Pu) phase, less oxygen-stabilized α-Zr in Alloy-C would suggest a Zr-rich δ-(U,Pu)Zr_2 phase compared to that of Alloy-A. Silcock [13] and Barnard [14] observed a hexagonal structure with $a_0 = 5.03$ Å and $c_0 = 3.08$ Å for the δ-UZr_2 phase. The trend is toward a larger lattice parameter with increasing Zr content within the binary U–Zr system [10]. In fact, this is the trend observed with Alloy-C (proposed Zr-rich) having larger δ-(U,Pu)Zr_2 lattice parameters and no γ-U compared to the smaller δ-(U,Pu)Zr_2 lattice parameters and presence of γ-U for Alloy-A. Alloy-B had a much larger ζ-(U,Pu) lattice parameter compared to Alloys-A and -C, suggesting that the phase was even more U-lean. Because a comparable amount of oxygen-stabilized α-Zr was observed in the photomicrograph for Alloy-B, and δ-(U,Pu)Zr_2 lattice parameters were comparable to those of Alloy-A, it is expected that Alloy-B contains less δ-(U,Pu)Zr_2 phase than predicted and a greater amount of γ-U, due to less Zr availability and excess U. The hypothesized trend is in fact observed with the quantitative phase measurements.

For the second set of alloys (Alloys-D, -E, and -F), the amount of δ-(U,Pu)Zr_2 increased while the amount of ζ-(U,Pu) decreased with increased Zr contents. A minimal change in the major phase compositions was observed with variations in U and Pu concentrations for these three alloys. Observation of the photomicrographs in Fig. 1 shows that Alloys-D and -E had minor amounts of oxygen-stabilized α-Zr (similar to that observed for Alloy-C), while Alloy-F had none apparent. The lattice parameter determinations for Alloys-D and -F are similar and very close to those of Lawson et al., suggesting a composition very close to ζ-$Pu_{0.6}U_{0.4}$ [9]. The lattice parameter determination for the ζ-(U,Pu) phase of Alloy-E was slightly larger, suggesting a U-lean phase.

The U-lean ζ-(U,Pu) phase coupled with a small amount of Zr tied up as oxygen-stabilized α-Zr and is expected to result in slightly less δ-(U,Pu)Zr_2 phase. In fact, the determined amount of δ-(U,Pu)Zr_2 phase was 27 wt.%, very close to the predicted amount of 30 wt.%. For Alloy-E, the excess U is present as α-U and γ-U. Alloys-D and -F had the most variation between measured phase content and predicted phase content. The lattice parameters were close to ζ-$Pu_{0.6}U_{0.4}$ for both alloys, but Alloy-F had smaller lattice parameters for the δ-(U,Pu)Zr_2 phase compared to all other alloys, suggesting a Zr-depleted phase.

In general, the transition temperature for the $\delta+\zeta\rightarrow\delta+\zeta+\gamma$ transition, Alloys-A, -B, and -C, increased with decreasing amounts of Pu and increasing amounts of U, from 815 K for Alloy-C (34 wt.% Pu) to 833 K for Alloy-A (20 wt.% Pu). For Alloy-D, the transition temperature increased back to 820 K, with a subsequent drop in Pu (and corresponding increase in U and Zr content) from Alloy-C. The three-phase mixture is predicted to consist of approximately 55% δ-(U,Pu)Zr_2, 30% ζ-(U,Pu), and 15% γ-U for Alloys-B and -C at 823 K, according to the U–Pu–Zr ternary phase diagram in Fig. 2. Although Alloys-B and -C are close in reduced composition, Alloy-B had much less δ-(U,Pu)Zr_2 phase than predicted (28 wt.%) in the as-cast alloy and a significant amount of γ-U (13 wt.%), while Alloy-C was close in predicted composition (50 wt.% δ-(U,Pu)Zr_2) and no γ-U present in the as-cast structure.

Thus, the trend suggests that the $\delta+\zeta\rightarrow\delta+\zeta+\gamma$ transition for Alloy-B is mainly associated with the conversion of ζ to δ, while that of Alloy-C is associated with the conversion of ζ to γ. Alloy-A contained slightly less δ-(U,Pu)Zr_2 than predicted (6 wt.%), but also contained 8 wt.% γ-U in the as-cast structure. At 853 K, Alloy-A is predicted to consist of approximately 15% δ-(U,Pu)Zr_2, 55% ζ-(U,Pu), and 30% γ-U. Similar to Alloy-C, the $\delta+\zeta\rightarrow\delta+\zeta+\gamma$ transition for Alloy-A is mainly associated with the conversion of ζ to γ, with very little of the ζ transforming into δ. Alloy-D contained 89 wt.% δ-(U,Pu)Zr_2 compared to a predicted 65 wt.%. At 823 K, Alloy-D is predicted to consist of approximately 65% δ-phase, 20% ζ-phase, and 15% γ-phase. The transition for this alloy is associated with the transition of δ into ζ and γ, and had the lowest enthalpy

of transition out of the alloys that underwent this transition. Thus, it appears that the enthalpy associated with a ζ to δ conversion is greater than that of a ζ to γ conversion, because Alloy-B had twice the enthalpy of Alloys-A or -C for this particular phase transition. In addition, the enthalpy of transition from δ to ζ or γ is about half that of ζ to γ.

For the same four alloys, the $\delta + \zeta + \gamma \rightarrow \zeta + \gamma$ transition temperature increased with increasing amounts of U, ranging from 832 K for Alloy-D to 920 K for Alloy-A. The enthalpy of transition was similar for Alloys-A and -B (8 J g^{-1}), decreased by over half with increased Pu (Alloy-C), and increased back to 10 J g^{-1} with increased Zr along with decreased U and Pu (Alloy-D). The difference in enthalpy between Alloy-B and Alloy-C in which both contained 20 wt.% Zr is much greater than the difference in enthalpy between Alloy-B and Alloy-A. At 853 K, Alloys-B and -C are predicted to consist of approximately 65% γ-U and 35% ζ-(U,Pu), while at 868 K, Alloy-A is predicted to consist of 55% γ-U and 45% ζ-(U,Pu). For Alloys-B and -C, all the δ-(U,Pu)Zr_2 has transformed into mostly γ-U, although Alloy-B most likely had less δ-phase than Alloy-C. For Alloy-A, all of the δ-(U,Pu)Zr_2 and some of the ζ-(U,Pu) has transformed into γ-U. It is possible that Alloy-B required some additional ζ-(U,Pu) transition into γ in this temperature range given the δ-phase deficiency to start.

Similarly, the conversion of δ into γ for Alloy-A is accompanied by transition of some of the ζ. At 853 K, Alloy-D is mainly γ-U, with a very minor amount of ζ-phase. Thus, all the δ and most of the ζ have transformed to γ. It appears that the enthalpy of transition associated with δ and ζ into γ is larger than that of mostly δ into γ, as is the case for Alloy-C that had the lowest enthalpy of transition for all four alloys.

Finally, the $\zeta + \gamma \rightarrow \gamma$ transition temperature increased with increasing U, ranging from 855 K for Alloy-D to 933 K for Alloy-A. The enthalpy of this transition increased with decreasing amounts of Pu for Alloys-A, -B, and -C. The increase was minor between Alloys-B and -C, owing to the similarity in composition (varying only by 3 wt.% Pu and U). The enthalpy of Alloys-B and -C effectively doubled Alloys-A and -D. Alloy-A contained a significantly greater amount of U while Alloy-D contained a significantly greater amount of Zr. The larger enthalpy for Alloy-A is expected given the greater amount of ζ-phase. For Alloy-D, the trend is not expected, and in general, there was significant disagreement in enthalpy values from heating and cooling the alloy. The reason for the disagreement is not known or easily explained at this time, but could be effectively dealt with by slowing the heating rate of the sample and by using a higher thermal conductivity gas, e.g., helium.

Of the six alloys, Alloy-F went through the most transitions. Between 773 and 823 K, the $\delta + \zeta$ begins to transition to $\delta + \zeta + \eta$, containing mostly the δ-(U,Pu)Zr_2 phase. At 853 K, the $\delta + \zeta + \eta$ begins to transition to $\delta + \gamma$, composed of mostly γ-phase. By 868 K, the remaining δ has transitioned into γ-phase. The enthalpies associated with the first two transitions are double the enthalpy of the final transition. This suggests that the enthalpies associated with transformation of ζ into η and $\zeta + \eta$ into γ are higher than the enthalpies associated with the transformation of δ into γ. More analysis and additional samples need to be performed in this composition range to ensure that the proposed behavior is correct.

5. Conclusions

Metallic fuel alloys are under consideration for the transmutation of minor actinides in fast reactors. Characterization activities, specifically thermal and phase analyses are being conducted as part of the fuel development campaign for these considerations. In particular, thermal and phase analyses have been conducted on six proposed fuel alloys, each containing varying amounts of U, Pu, Am, Np, and Zr. The four- or five component systems have been reduced into a ternary U–Pu–Zr system in order to predict behavior. Such a reduction proved relatively accurate, given the small amounts of Am and Np present in the alloys, and analysis revealed the following conclusions:

- Rietveld refinement of the XRD measurements performed on as-cast samples at room temperature are very close to those predicted by a constructed room temperature U–Pu–Zr ternary phase diagram.
- The amount of oxygen-stabilized α-Zr has an impact on the phase distribution and assemblage of the as-cast alloys. Increased amounts of oxygen-stabilized α-Zr tend to result in a U-lean ζ-(U,Pu) phase, less δ-(U,Pu)Zr_2 phase than predicted, and increased amounts of non-equilibrium γ-U.
- Transition temperatures tend to be strongly influenced by U content, increasing with increased amounts of U in the alloy, and less influenced by Pu content. There is a secondary, but minor, dependence of transition temperature on Zr content.
- Enthalpies associated with transitions have a strong dependence on the amounts of δ-(U,Pu)Zr_2 and ζ-(U,Pu) phases present in the as-cast alloy. Transitions associated with the δ-(U,Pu)Zr_2 phase into another phase tend to result in greater enthalpy values than those associated with ζ-(U,Pu), η-phase, or γ-U.

Acknowledgements

Work supported by the US Department of Energy, Office of Nuclear Energy (NE), under DOE Idaho Operations Office Contract DE-AC07-05ID14517. The authors are especially grateful to the Analytical Laboratory (AL) and Fuel Manufacturing Facility (FMF) staff. The authors wish to specifically acknowledge Mr. Andrew Maddison, Dr. Steven Frank, Mr. Timothy Hyde, Mr. Jim Stuart, Dr. Leah Squires, Mr. Jim Morrison, Mr. Scott Wilde, Mr. Benjamin Krause, and Dr. Marsha Lambregts, for their assistance with fabrication, sample preparation, and material transfers related to these experiments. Finally, the authors would like to acknowledge the Health and Physics staff for their continued support of this work in the AL and FMF facilities.

References

[1] D. Mohr, L.K. Chang, E.E. Feldman, P.R. Betten, H.P. Planchon, Nucl. Eng. Des. 101 (1) (1987) 45–56.
[2] D.E. Burkes, R.S. Fielding, D.L. Porter, D.C. Crawford, M.K. Meyer, J. Nucl. Mater. 389 (2009) 458–469.
[3] T. Hyde et al., Fabrication Report for the AFC-2A and AFC-2B Capsule Irradiations in the ATR, Idaho National Laboratory, 2007, INL/EXT-13021.
[4] J.R. Kennedy, D. Janney, The Phase and Microstructure Characterization of AFC-2A Metallic Transmutation Fuels: FY2007 Report, Idaho National Laboratory, 2007, INL/EXT-13027.
[5] J.R. Kennedy, D.D. Keiser Jr., S.M. Frank, The Microstructure and Phase Characterization of Low-fertile AFC-1F Metallic Transmutation Test Fuels: Final Report, Idaho National Laboratory, 2004.
[6] D.R. O'Boyle, A.E. Dwight, in: Proc. Fourth Int. Conf. on Pu and Other Actinides, Santa Fe, NM, 1970, p. 720 (Session 2).
[7] T. Ogawa, J. Alloys Compd. 194 (1) (1993) 1–7.
[8] T.B. Massalski (Ed.), Binary Alloy Phase Diagrams, second ed., vol. 3, ASM International, 1990.
[9] A.C. Lawson, J.A. Goldstone, B. Cort, R.J. Martinez, F.A. Vigil, T.G. Zocco, J.W. Richardson Jr., M.H. Mueller, Acta Crystallogr. Sect. B: Struct. Sci. 52 (1) (1996) 32–37.
[10] M. Akabori, A. Itoh, T. Ogawa, F. Kobayashi, Y. Suzuki, J. Nucl. Mater. 188 (1992) 249–254.
[11] R.D. Fraser, E. Suzuki, Anal. Chem. 41 (1) (1969) 37–39.
[12] F.H. Ellinger, R.O. Elliott, E.M. Cramer, J. Nucl. Mater. 1 (3) (1959) 233–243.
[13] J. Silcock, Trans. AIME 209 (1957) 521.
[14] R.D. Barnard, Proc. Phys. Soc. 78 (5) (1961) 722–727.